

Simulating complex networks in phase space: Gaussian boson sampling

Peter D. Drummond, Bogdan Opanchuk, A. Dellios and Margaret D. Reid
Swinburne University of Technology, Melbourne 3122, Australia

We show how phase-space simulations of Gaussian quantum states in a photonic network permit verification of measurable correlations of Gaussian boson sampling (GBS) quantum computers. Our results agree with experiments for up to 100-th order correlations, provided decoherence is included. We extend this to more than 16,000 modes, and describe how to simulate genuine multipartite entanglement.

Bosonic quantum networks are increasingly useful in quantum technology and quantum computing applications [1]. Linear networks driven either by nonclassical number state [2–8] or Gaussian inputs [9–12] for boson sampling are becoming widely available. The squeezed-state interferometer, which is a two-mode linear network, is being employed to enhance gravitational-wave detection sensitivity [13, 14]. More complex photonic networks are under development, both as novel interferometers [15, 16] and as test-beds for multipartite entanglement [17–19]. Other examples include the Ising machine, used to solve large NP-hard optimization problems [20–22].

A dramatic increase in scale of a boson sampling quantum network has recently been achieved. Zhong et al [23] implemented a 100-mode Gaussian boson sampler (GBS) with squeezed inputs, and detected the output photon counts, whose distribution is called the 'Torontonian'. They measured up to 76-th order coincidence counts in the outputs, which they estimated to take 0.6 billion years to simulate conventionally on the world's fastest current supercomputer. This has led to reports of quantum supremacy by Zhong et al: that is, a quantum device implementing a computational task that is not classically feasible [24, 25]. Similar reports have been made with smaller experiments using quantum logic gates [26].

There is an ongoing debate on how to rigorously validate such technology [27, 28]. Validation based on low-order correlations [29] or direct classical simulation may be susceptible to mock-ups. The difficulty is clear: without classical benchmarks, how can one know what output is expected, in order to verify the experiments?

Quesada et al [11, 30] explain that classical evaluation or simulation of the Torontonian distribution is exponentially complex, making it nearly impossible for correlations of more than 50-th order [31]. Exponential complexity therefore leads to theoretical challenges for validation. Gaussian inputs to linear networks [9, 32] have a non-computable discrete count probability for large mode number, the Hafnian [10] or in the saturable detector case, the Torontonian [11].

In this Letter, we show how one may in part solve this problem, by simulating Gaussian boson linear networks in *quantum phase-space*, using extra dimensions. This provides a way to verify the output measurable quantum correlations. The experiment is not *directly* simu-

lated using discrete photon counts [11, 30]. Rather, we verify observable, binned correlations by averaging over many random trajectories in phase space [33]. Despite quantum complexity, these have the same correlations as experiments. By contrast, an explicit simulation with discrete counts is only feasible either for small networks or with large decoherence [34]. Our methods provide a way to certify the measurable outputs of experiments, even for systems much larger than current ones.

We have computed *all* of the grouped correlations measured by Zhong et al [23], including 76-th order coincidence counts, as well as more detailed correlations present in their data. Our phase-space simulations agree extremely well with experimental grouped count distributions [23], after including additional decoherence effects, and are scalable. Chi-squared statistical tests are utilized, as in other sparse random-number generation testing [35, 36]. These show an improvement of two orders of magnitude for fitting theoretical 100-th order correlations to experiment, when decoherence is included.

Predictions are also obtained for up to 16000-th order correlations, taking minutes, while computing the Torontonian would take $\sim 10^{4800}$ years with some methods. With our approach, computational times and sampling errors are comparable to those in experiments for the same number of samples, making them useful for validation of GBS experiments. We can efficiently compute the marginal, low-order correlations proposed earlier, as well as higher order measurable correlations.

Boson sampling data has some of the properties of mathematical 'trapdoor' functions [37]. These outputs are hard to generate numerically, but we demonstrate how any measurable correlation or moment can be verified. As methods used to detect eavesdroppers involve measurement of moments, this also suggests relevance to cryptographic applications. We further demonstrate, using moments simulated in quantum phase-space, how to certify the genuine M -partite entanglement of all $M = 100$ nodes of a Gaussian network.

Two common phase-space approaches are used: the generalized P-representation [38] and the Wigner representation [39]. These methods do not assume gaussianity, and applications to non-Gaussian photonic networks were already demonstrated [33, 40]. P-representations are most useful for simulating GBS devices, as they do

not include vacuum noise, making them efficient for sampling photo-detection measurements. The Wigner representation is better for analyzing multipartite entanglement, with data coming from quadrature measurements [41–43], which also have been carried out at an increasingly large scale [17–19, 44, 45].

We consider an M mode bosonic network, with squeezed-state inputs to N out of M modes. A linear, unitary transformation is made to a set of M output modes, combined with decoherence and losses. Measurements are carried on the output state $\hat{\rho}^{(\text{out})}$. The theoretical problem is to calculate observables from the output quantum state. To solve this, we utilize discrete Fourier transform methods for ensemble averages of grouped photon counts [33].

A squeezed-state is a minimum uncertainty state in which one of the input mode quadratures has its fluctuations reduced below the vacuum noise level [46, 47]. We suppose that the squeezing of $\hat{\rho}^{\text{in}}$ for each excited mode is in the imaginary part of $\boldsymbol{\alpha}$. If each input is independent, the quantum state can be factorized into a product of single-mode states. Defining input quadrature operators $\hat{x}_j^{\text{in}} = \hat{a}_j^{\text{in}} + \hat{a}_j^{\text{in}\dagger}$, $\hat{p}_j^{\text{in}} = (\hat{a}_j^{\text{in}} - \hat{a}_j^{\text{in}\dagger})/i$, so that $[\hat{x}_\ell^{\text{in}}, \hat{p}_j^{\text{in}}] = 2i\delta_{\ell j}$, the quantum inputs are defined by a squeezing vector $\mathbf{r} = [r_1, \dots, r_N]$. The variances in each mode are:

$$\begin{aligned} \langle (\Delta \hat{x}_j^{\text{in}})^2 \rangle &= 1 + \gamma_j = e^{2r_j} \\ \langle (\Delta \hat{p}_j^{\text{in}})^2 \rangle &= (1 + \gamma_j)^{-1} = e^{-2r_j}. \end{aligned} \quad (1)$$

The input photon numbers are $n_j = \sinh^2(r_j)$, with coherences of $m_j = \langle \hat{a}_j^2 \rangle = \sinh(r_j) \cosh(r_j)$.

At large M , number state expansions require exponentially many expansion coefficients to treat this. Instead, we use phase-space expansions [48] which allow a probabilistic representation of input states. An efficient technique for photon-counting measurements is the generalized P-representation [38, 49]. This has been applied to other large-scale bosonic simulations [50].

The quantum density matrix $\hat{\rho}$ is expanded over a subspace of the complex plane defined by:

$$\hat{\rho}^{\text{in}} = \Re \int \int P(\boldsymbol{\alpha}, \boldsymbol{\beta}) \hat{\Lambda}(\boldsymbol{\alpha}, \boldsymbol{\beta}) d\mu(\boldsymbol{\alpha}, \boldsymbol{\beta}). \quad (2)$$

The operator basis $\hat{\Lambda}$ is a coherent state projector onto multimode Glauber [51] coherent states, and $d\mu(\boldsymbol{\alpha}, \boldsymbol{\beta})$ is an integration measure on the $2M$ -dimensional complex space of amplitudes $\boldsymbol{\alpha}, \boldsymbol{\beta}$. For a squeezed input state $\hat{\rho}^{(\text{in})}$, one obtains a positive distribution on a real subspace with $(\boldsymbol{\alpha}, \boldsymbol{\beta}) = (\mathbf{x}, \mathbf{y})$, $d\mu(\boldsymbol{\alpha}, \boldsymbol{\beta}) = dx dy$. If the input is $\hat{\rho}_{1S} \equiv \prod_j |r_j\rangle \langle r_j|$, a product of single-mode squeezed state density matrices, then the following solution for a squeezed state always exists, based on one-

dimensional coherent state expansions [52]:

$$P(\mathbf{x}, \mathbf{y}) = \prod_j C_j e^{-(x_j^2 + y_j^2)(\gamma_j^{-1} + 1/2) + x_j y_j}, \quad (3)$$

where the normalization constant can be obtained to be $C_j = \sqrt{1 + \gamma_j}/(\pi\gamma_j)$.

In this approach, normally ordered operator moments are equivalent to stochastic moments [38], so that $\langle \hat{a}_{j_1}^\dagger \dots \hat{a}_{j_n} \rangle = \lim_{S \rightarrow \infty} \langle \beta_{j_1} \dots \alpha_{j_n} \rangle_P$, with quantum expectation values denoted $\langle \rangle$, and probabilistic averages with S samples denoted $\langle \rangle_P$.

To create input samples with the Gaussian distribution $P(\mathbf{x}, \mathbf{y})$, one can generate real Gaussian noises with $\langle w_i w_j \rangle_P = \delta_{ij}$, together with corresponding random phase-space samples where $\vec{\alpha} = [\boldsymbol{\alpha}, \boldsymbol{\beta}] = [\alpha_1, \dots, \alpha_{2M}]$. The stochastic model for a pure state, $[\boldsymbol{\alpha}^0, \boldsymbol{\beta}^0]$ is given by [53]:

$$\begin{aligned} \alpha_j^0 &= \delta_{j+} w_j + \delta_{j-} w_{j+M} \\ \beta_j^0 &= \delta_{j+} w_{j+M} + \delta_{j-} w_j. \end{aligned} \quad (4)$$

The real coefficients $\delta_{j\pm}$ must satisfy $(\delta_{j+}^2 - \delta_{j-}^2)^2 = 2\delta_{j+}\delta_{j-} = n_j$, and the solution is $\delta_{j\pm}^2 = \frac{1}{2}(m_j \pm \sqrt{n_j})$.

Pulsed squeezing [54] involves multiple longitudinal modes, with mismatches in time or frequency [23], as well as phase noise [53]. We model the experimental decoherence approximately by an intensity transmissivity $T = 1 - \epsilon$ into the network, together with a thermal input of $n_j^{\text{th}} = \epsilon n_j$ uncorrelated photons per mode. This is similar to thermal squeezing models [55], except with an invariant photon number.

In the generalized P-representation, the result of this decoherence model is to add thermal noise, so that:

$$\begin{aligned} \alpha_j &= \sqrt{T}\alpha_j^0 + \sqrt{n_j^{\text{th}}/2}(w_{k+2M} + iw_{k+3M}) \\ \beta_j &= \sqrt{T}\beta_j^0 + \sqrt{n_j^{\text{th}}/2}(w_{k+2M} - iw_{k+3M}). \end{aligned} \quad (5)$$

Other possible phase-space methods include the s -ordered classical bosonic representations [56]. Of these, the Wigner [57] and Q-function [58], with symmetric and anti-normal ordering respectively, have additional vacuum noise. These give exponentially larger sampling errors [53] for intensity correlations, while the Glauber P-representation is singular for squeezed states. They have a classical phase-space, in which $\beta_j = \alpha_j^*$.

In our definition of s -ordering, we use the s parameter signifying the relative amount of vacuum noise, with $s = 0$ for normal ordering, $s = 1/2$ for symmetric ordering, and $s = 1$ for anti-normal ordering. For pure state squeezed state inputs [59], the s -ordered classical phase-space stochastic amplitude is $\alpha_j^0 = d_{j+} w_j + id_{j-} w_{j+M}$, where $d_{j\pm}$ has the requirement:

$$\begin{aligned} d_{j+}^2 + d_{j-}^2 &= \sinh^2(r_j) + s \\ d_{j+}^2 - d_{j-}^2 &= \cosh(r_j) \sinh(r_j). \end{aligned} \quad (6)$$

Solving, one finds that $d_{j\pm} = \frac{1}{2}\sqrt{e^{\pm 2r_j} - 1 + 2s}$. The amplitude α_j^0 is attenuated and added to a thermal field n_j^{th} as before, this time with a coefficient of $\sqrt{n_j^{th} + \epsilon s}$ to preserve commutators.

Once a set of input states is simulated, it can be transformed and used to sample the output state in any of these representations. An input density matrix $\hat{\rho}^{(in)}$ is changed by a linear photonic network to an output density matrix $\hat{\rho}^{(out)}$. For unitary transformations \mathbf{T} , the phase-space amplitudes are transformed deterministically, where $\boldsymbol{\alpha}' = \mathbf{T}\boldsymbol{\alpha}$, $\boldsymbol{\beta}' = \mathbf{T}^*\boldsymbol{\beta}$, in all representations. In the generalized P-representation one may include a non-unitary transmission matrix to take account of losses, which is equivalent to a master equation [60].

For normal ordering in a linear network, the output density matrix has an exceptionally simple form [61], including linear couplings and losses:

$$\hat{\rho}^{(out)} = \Re \int \int P(\boldsymbol{\alpha}, \boldsymbol{\beta}) \hat{\Lambda}(\mathbf{T}\boldsymbol{\alpha}, \mathbf{T}^*\boldsymbol{\beta}) d\mu(\boldsymbol{\alpha}, \boldsymbol{\beta}). \quad (7)$$

Here the input distribution $P(\boldsymbol{\alpha}, \boldsymbol{\beta})$ is no longer restricted to the real axes, if there are input thermal photons included to model decoherence with $\mathbf{n}^{th} \neq 0$.

Highly efficient photo-detectors saturate for more than one count at a detector. The projection operator for each detector is $\hat{\pi}_j(c_j)$, where $c_j = 0, 1$ is the number of measured counts at the j -th detector. As this operator is normally ordered, the corresponding phase-space observable is

$$\pi_j(c_j) = e^{-n'_j} \left(e^{n'_j} - 1 \right)^{c_j}. \quad (8)$$

Here $n'_j = \alpha'_j \beta'_j$ is the output number variable, sampled with probability $P(\boldsymbol{\alpha}, \boldsymbol{\beta})$, corresponding to the number operator $\hat{a}_j^{\dagger out} \hat{a}_j^{out}$.

Experimental results are given by a count vector of binary numbers \mathbf{c} . This is a complex point pattern, with up to 2^M possible patterns available. For a set S of M_s sites, each pattern \mathbf{c} has an M_s -order correlation operator of

$$\hat{\Pi}_S(\mathbf{c}) = \bigotimes_{j \in S} \hat{\pi}_j(c_j). \quad (9)$$

The expectation, $\langle \hat{\Pi}_S(\mathbf{c}) \rangle$ is the Torontonian function [11] for Gaussian inputs, if the set of sites S corresponds to all M output channels. In all cases, the corresponding M_s -th order moment is simulated by replacing $\hat{\pi}_j$ with the randomly sampled c-number π_j .

As there are exponentially many possible count patterns \mathbf{c} , the probability of measuring any individual pattern, $\langle \hat{\Pi}_S(\mathbf{c}) \rangle$, is infinitesimal for large M_s . A direct measurement cannot obtain all such correlations in less than exponential time. This is the certification problem

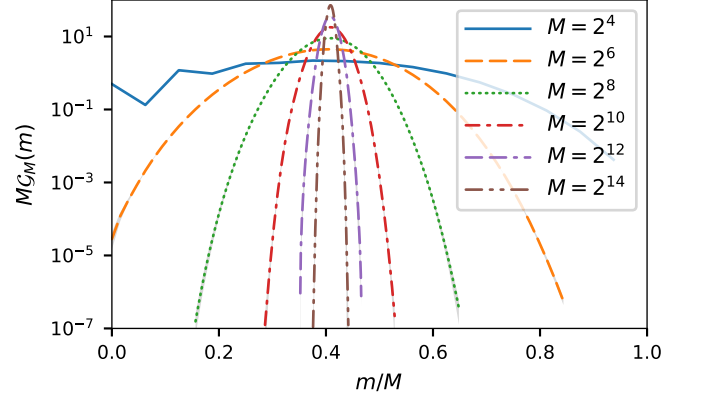


Figure 1. Theoretical scaling of total grouped count distribution with M . Results are for $MG_M^{(M)}(m)$ vs m/M , for $\mathbf{r} = 1$, $\mathbf{n}^{th} = 0$, $N = M/2$ and random unitaries. Mode numbers were $M = 2^4, 2^6, 2^8, 2^{10}, 2^{12}, 2^{14}$, with sample numbers of $S = 10^8, 10^6, 10^5, 1.6 \times 10^4, 4 \times 10^3, 2 \times 10^3$ respectively. Grey shading indicates sampling errors.

with boson sampling. It is exponentially hard to calculate all moments. It is also exponentially hard to *measure* them [33, 40].

Grouped counts are therefore essential for verifying statistics at large M . One must simulate and measure the n -th order grouped correlations, $\mathcal{G}_M^{(n)}(\mathbf{m})$, where $n = \sum_{j=1}^g M_j \leq M$, is the total correlation order [51], and:

$$\mathcal{G}_M^{(n)}(\mathbf{m}) = \left\langle \prod_{j=1}^g \left[\sum_{c_i=m_j} \hat{\Pi}_{S_j}(\mathbf{c}) \right] \right\rangle. \quad (10)$$

These are the grouped count correlations. They are the probability of observing $\mathbf{m} = (m_1 \dots m_g)$ grouped counts in disjoint sets S_1, S_2, \dots of $\mathbf{M} = (M_1, M_2, \dots)$ output modes. For the case of $n < M$, these include low-order marginal correlations previously proposed for verification purposes, with $M - n$ outputs ignored. The first-order correlation with $n = 1$, $M_j = \delta_{jm}$ is the count probability in the m -th channel. Similarly, $n = M$ and $\mathbf{M} = (1, 1, \dots)$ gives the Torontonian. Finally, $MG_M^{(M)}(m)$ is the probability for observing m clicks in any pattern, as reported in recent experiments [23].

This appears intractable at first: how can one compute the sum of exponentially many terms, if each is exponentially hard? Yet, high-order correlations are readily simulated on replacing the operator $\hat{\pi}_j$ by the phase-space variable π_j , and averaging over the probability $P(\boldsymbol{\alpha}, \boldsymbol{\beta})$. The summation over grouped correlations is achieved through introducing angles $\theta_i = 2\pi/(M_i + 1)$, with a Fourier observable $\tilde{\mathcal{G}}$ defined for $k_i = 0, \dots, m_i$, as:

$$\tilde{\mathcal{G}}_M^{(n)}(\mathbf{k}) = \left\langle \prod_{j=1}^g \bigotimes_{i \in S_j} (\pi_i(0) + \pi_i(1) e^{-ik_i \theta_i}) \right\rangle_P. \quad (11)$$

The binned correlation is then obtained from a multi-dimensional inverse discrete Fourier transform, giving

$$\mathcal{G}_M^{(n)}(\mathbf{m}) = \frac{1}{\prod(M_i + 1)} \sum_{\mathbf{k}} \tilde{\mathcal{G}}_M^{(n)}(\mathbf{k}) e^{i \sum k_i \theta_i m_i}. \quad (12)$$

All combinations of terms vanish in the inverse Fourier transform *except* those terms with \mathbf{m} counts. This algorithmic procedure is highly scalable. Two simulation codes were written and tested. Exact Torontonians were simulated for small networks. Analytically tractable inputs were used to test large networks. Excellent agreement was found in all cases, as described in the Supplemental Material.

To demonstrate this, we graph the grouped count probability in Fig (1) for sizes up to $M = 16,000$, using squeezed states with $r = 1$, $\epsilon = 0$, for $N = M/2$ inputs, and random unitaries. The main computational limitation is the time and storage (4GB) required for the largest matrix. The approach can be used to grouped correlations with a chi-squared test [62], provided the usual requirement of at least 5-10 counts per bin is satisfied [36, 63], so that there are Gaussian error distributions.

The grouped correlations provide a signature of a quantum state. For them to be useful, they must be measurable and have a low sampling error. To validate results, the theoretical sampling error E_t must be less than the experimental sampling error E_e . Just as with the simulations, the experimental sampling errors depend on the number of samples used, and scale as $E_e \propto c_e S_e^{-1/2}$. We find that experiment and theory have similar time-scales, for comparable error-bars.

Due to internal averaging, single group measures are less sensitive to the unitary as n increases, but are very sensitive to decoherence. Count “fingerprints” with more groups are also needed for a complete test, and one is computed below. Many such measures are available, both from experimental data and from simulations.

To compare theory to experiment, squeezing vectors and transmission data from a recent 100-mode Gaussian boson sampling experiment were obtained [23] and simulated with 1.2×10^6 samples. The data was a 50 mode vector of amplitudes \mathbf{r} , a 50×100 transmission matrix \mathbf{T} , and 5×10^7 measured click patterns. Details of the statistical methods, the tests of the simulation codes, and further results are given in the Supplemental Material.

Simulating *total* counts, $\mathcal{G}_M^{(M)}(m)$, with pure squeezed-state inputs gave a large chi-squared value $\chi_c^2/k = 2.1 \times 10^3 \gg 1$, with $k = 63$ valid data points. Additionally, we tested a 100 mode fully thermalized model. This gave an even larger discrepancy. The normalized chi-squared value was $\chi_{th}^2/k = 3.6 \times 10^4 \gg 1$, confirming a prediction [64] that one can readily distinguish boson sampling from uniform distributions.

Better agreement with experiment was obtained with a small admixture of thermal inputs. For optimal fitting,

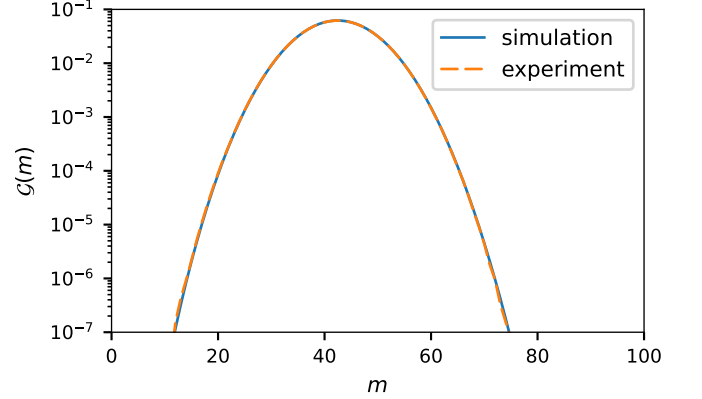


Figure 2. Comparison of theory with experiment of $\mathcal{G}_{100}^{(100)}(m)$, for a 100 channel GBS total count distribution. Solid line is the theoretical prediction with $\epsilon = 0.138$ relative decoherence and 1.2×10^6 samples. The dotted line is the experimental data obtained from 5×10^7 samples.

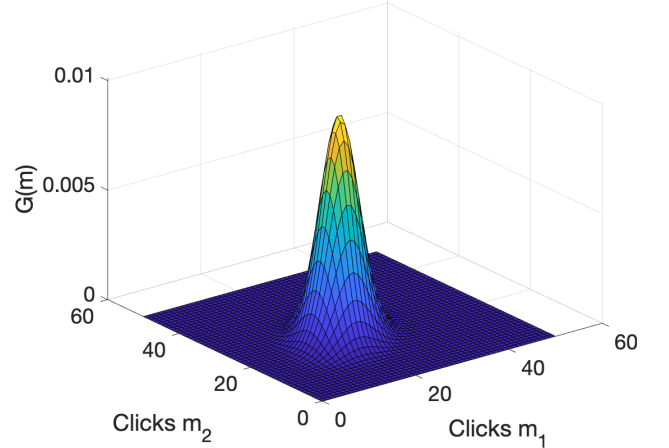


Figure 3. Simulation of a 100 channel GBS count distribution binned into two dimensions, $\mathcal{G}_{50,50}^{(100)}(\mathbf{m})$, with 1.2×10^6 samples. Differences between theory and experiment were negligible on the scale shown.

we included an $\epsilon = 0.138$ thermal photon component to model longitudinal mode mismatching, and a transmission amplitude increased by .063%. Results of simulations are given in Fig (2). This agrees with experiment over a range of six orders of magnitude in the measurable grouped probabilities. A normalized chi-squared value of $\chi_{\epsilon}^2/k = 1.27 = O(1)$, was obtained, showing excellent agreement up to statistical errors. This gave two orders of magnitude lower chi square values than with pure state inputs.

Fig (3) shows $\mathcal{G}_{50,50}^{(100)}(\mathbf{m})$, which is a two-dimensional binning of the 100-th order correlations. Any number of bins - up to M - are feasible in principle, although both computational overheads and experimental sampling er-

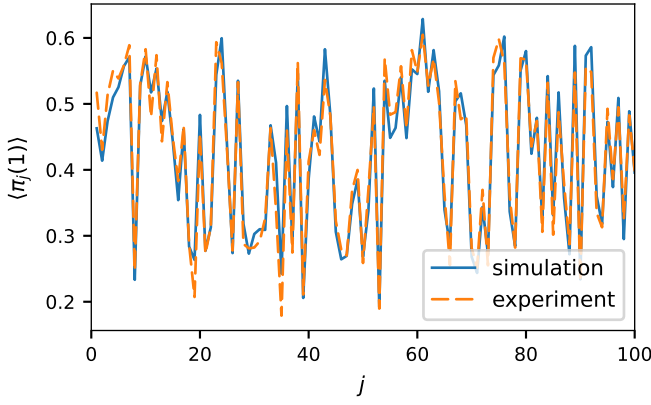


Figure 4. Comparison of theory vs experiment for a 100 channel GBS count probability per channel, $\mathcal{G}_{\delta_j}^{(1)}(1) \equiv \langle \hat{\pi}_j(1) \rangle$, versus mode j . Solid line is the theory with with $\epsilon = 0.138$ relative decoherence, dotted line obtained from 5×10^7 experimental data records. Computational sampling errors with 1.2×10^6 samples were negligible on this scale.

rors increase as the group number increases. As another comparison, the marginal count probability per channel $\mathcal{G}_{\delta_j}^{(1)}(1) = \langle \pi_j(1) \rangle$, is graphed in Fig (4). This shows good agreement with experiment, although with less dependence on decoherence than in high-order correlations. The chi-squared values were higher in these two cases, due to uncompensated errors in reported data. These 100 mode, million sample phase-space simulations take ~ 100 s on a desktop computer.

We finally consider a different type of measurement, to answer the question of how to identify multipartite entanglement [42]. A route to achieving multipartite entanglement is to first generate a two-mode Einstein-Podolsky-Rosen (EPR) correlated state [65], using two squeezed inputs on a beam splitter. One output is then passed through a further $M - 2$ beam splitters to generate M output fields \hat{a}_i^{out} [41, 43]. The first two inputs are orthogonally squeezed vacuum states: \hat{a}_2^{in} with $\Delta^2 \hat{x}_2^{in} = e^{-2r}$, and \hat{a}_1^{in} with $\Delta^2 \hat{p}_1^{in} = e^{-2r}$. All other inputs are vacuum states. The inputs \hat{a}_1^{in} and \hat{a}_2^{in} are combined across a beam splitter, with reflectivity R_1 , according to

$$\begin{aligned} \hat{a}_1^{(1)} &= \sqrt{R_1} \hat{a}_1^{in} + \sqrt{1 - R_1} \hat{a}_2^{in} \\ \hat{a}_2^{(1)} &= \sqrt{1 - R_1} \hat{a}_1^{in} - \sqrt{R_1} \hat{a}_2^{in} \end{aligned} \quad (13)$$

($R_1 = 1/2$). The two output fields $\hat{a}_i^{(1)}$ are EPR correlated, meaning that variances in both $\hat{x}_1^{(1)} - \hat{x}_2^{(1)}$ and $\hat{p}_1^{(1)} + \hat{p}_2^{(1)}$ become zero with infinite r . To generate tripartite entanglement, the output $\hat{a}_1^{(1)}$ is unchanged, but $\hat{a}_2^{(1)}$ is combined across a second beam splitter with reflectivity R_2 , and with a vacuum input $\hat{a}_3^{(in)}$, according to [41]. The three outputs of \hat{a}_i are written $\hat{a}_i^{(2)}$, $i = 1, 2, 3$. Continuing, the outputs $\hat{a}_1^{(2)} = \hat{a}_1^{(1)}$, $\hat{a}_2^{(2)}$ are unchanged, but

$\hat{a}_3^{(2)}$ is passed through a third beam splitter. It is possible to select the reflectivities of a string of beam splitters so that for final outputs $\hat{a}_i^{out} = \hat{a}_i^{(i)}$, $i = 1, \dots, M$

$$\begin{aligned} \xi_x &= \Delta^2(\hat{x}_1^{out} - \frac{1}{\sqrt{M-1}} \sum_{i>1}^M \hat{x}_i^{out}) = 2e^{-2r} \\ \xi_p &= \Delta^2(\hat{p}_1^{out} + \frac{1}{\sqrt{M-1}} \sum_{i>1}^M \hat{p}_i^{out}) = 2e^{-2r}, \end{aligned} \quad (14)$$

This is done on selecting for the k -th beam splitter, where $k = 1, \dots, M-1$, the reflectivity R_k , where $R_{M-1} = 1/2$, $R_{M-2} = \frac{1}{3}$, $R_{M-k} = 1/(k+1)$ for $k < M-1$, as explained in Refs. [41, 43], with $R_1 = 1/2$.

This result can be readily simulated, and we find that one can verify genuine M -partite entanglement at large M by establishing $\xi_x + \xi_p < 4/(M-1)$ [41, 43], as demonstrated in the Supplemental Material for $M=100$. The optimal simulation method is the Wigner representation, which for quadrature measurement is the natural approach, requiring no ordering corrections. Other methods gave larger sampling errors. As one might guess intuitively, it is optimal to use the representation that matches the measurement operator [66].

In summary, we have simulated Gaussian boson sampling with a positive P-representation method. This efficiently simulates large networks with nonclassical inputs and decoherence. Up to $M = 2^{14} = 16,384$ modes were treated as examples, with up to 16,000-th order correlations. There is excellent agreement with a recent 100-mode experiment for up to 100-th order correlations, with thermal decoherence included. More generally, the representation used should be targeted to the measurement. Positive P-representations are optimal for normal ordering, while Wigner representations scale better for quadrature measurements.

PDD thanks Jian-Wei Pan for access to essential experimental data. Large-scale calculations were performed on the OzSTAR national supercomputing facility funded by Swinburne University of Technology and the Australian National Collaborative Research Infrastructure Strategy (NCRIS). This work was also funded through an Australian Research Council Discovery Project Grant DP190101480, and a grant from NTT Research.

Supplemental material.

Simulating complex networks in phase space: Gaussian boson sampling

In this supplementary information, we give the technical details of the statistical tests and additional results used to obtain the data in the main paper.

STATISTICAL TESTS

Statistical tests are essential in comparing theory to experimental data in any area of science. Here, tests were used for comparing the phase-space simulation results both with exactly known distributions, and with 100 mode GBS experimental observations. The test procedures are similar in both cases. We use chi-square methods originally discovered by Pearson [62], which are widely used in probability and RNG validation [36, 63].

Chi-square tests are used to compare a theoretical probability distribution to a set of experimental measurements [62], and can also be used to compare two independent samples. In these tests, experimental observations are grouped into disjoint classes, with frequencies f_i (for $i = 1, 2, \dots, k$), from \mathcal{N}_e observations. Let an hypothesis \mathcal{H} give a probability P_i for an observation in the i -th class. The χ^2 value is:

$$\chi^2 = \sum_{i=1}^k \frac{(P_i \mathcal{N}_e - f_i)^2}{P_i \mathcal{N}_e}. \quad (15)$$

We note that this variable has a χ^2 distribution with $\langle \chi^2 \rangle / k = 1$, provided the counts all have a nearly Gaussian distribution. For our purposes, defining an experimental probability estimate as $P_i^e = f_i / \mathcal{N}_e$, this can be rewritten in an intuitive form as

$$\chi^2 = \sum_{i=1}^k \frac{(P_i^e - P_i)^2}{\sigma_{e,i}^2}. \quad (16)$$

Here, $\sigma_{e,i}^2 = P_i / \mathcal{N}_e \approx f_i / \mathcal{N}_e^2$ is the expected variance in the experimental counts, which will have Poissonian fluctuations. The count distribution is non-Gaussian for small counts. Hence, we ignore counts less than $f_i^{min} = 10$. By comparison, Knuth [36] suggests $f_i^{min} = 20$, and lower thresholds of $f_i^{min} = 5$ are recommended by NIST [63, 67]. However, changing thresholds has little effect.

In phase-space simulations, the true theoretical probability P_i is only available in the limit of large computational samples. It is non-Gaussian, due to the nonlinearity of moment calculations. The theoretical probability

P_i is therefore estimated numerically from its ensemble mean. This is computed [33] using an ensemble of sub-ensembles, each with large numbers of samples.

From the central limit theorem, sub-ensemble means are nearly Gaussian distributed, with a standard deviation of $\sigma_{s,i}$. These theoretical standard deviations are computed from the statistical fluctuations in the sub-ensemble means. As a result, the simulated ensemble mean P_i has a standard deviation in the mean of $\bar{\sigma}_{s,i} = \sigma_{s,i} / \sqrt{\mathcal{N}_s}$, where \mathcal{N}_s is the number of sub-ensembles, following standard results for Gaussian statistics.

This uncertainty in the true probability P_i implies that the chi-squared test needs to be modified. This case is almost identical to the well-known case of two samples drawn from the same population [35, 68]. Here, we have two distinct populations with identical moments, one discrete and one continuous. For a finite phase-space ensemble, we employ an error measure of:

$$\chi_s^2 = \sum_{i=1}^k z_i^2 = \sum_{i=1}^k \frac{(P_i - P_i^e)^2}{\sigma_i^2}. \quad (17)$$

This uses the fact that the experimental and simulated data are both independent and approximately Gaussian distributed. The difference in their means has a variance of $\sigma_i^2 = \sigma_{e,i}^2 + \bar{\sigma}_{s,i}^2$, which is obtained by adding the two variances. Since correlated fluctuations in the simulated P_i can modify the effective degrees of freedom, we do not calculate the detailed χ_s^2 distribution. Since $\lim_{\mathcal{N}_e, \mathcal{N}_s \rightarrow \infty} \langle \chi_s^2 \rangle / k = 1$, we simply verify that $\langle \chi_s^2 \rangle / k = O(1)$.

All fluctuations in the simulated data eventually vanish in the limit of a large simulation, because $\bar{\sigma}_{s,i}^2 \rightarrow 0$ as $\mathcal{N}_s \rightarrow \infty$. Such tests can therefore be applied to any experimental correlation, provided the measured data is grouped or binned to give enough counts to be significant. This requirement is far from unique to GBS, and moment tests are also used in other RNG tests [63], which have very similar requirements.

The difference between our tests and standard RNG tests is that the comparison moments are obtained through sampling. This is necessary because the exact Torontonian is effectively non-computable. However, it does raise the question of how many samples are needed. This is answered by increasing the sample number until $\bar{\sigma}_{s,i} < \sigma_{e,i}$. We found that $S = 1.2 \times 10^6$ was sufficient here, using 1200 sub-ensembles of 1000 samples.

To demonstrate our theoretical techniques, numerical code for simulations was written for two different languages (Matlab and Python) and computational platforms (a 14 core iMac Pro, and the Ozstar supercomputer with GPU hardware). Simulations were checked against known Torontonians for small 16-mode networks with squeezed inputs [11, 69].

We validated the theoretical code in larger cases by comparison to exact analytic results for squeezed, ther-

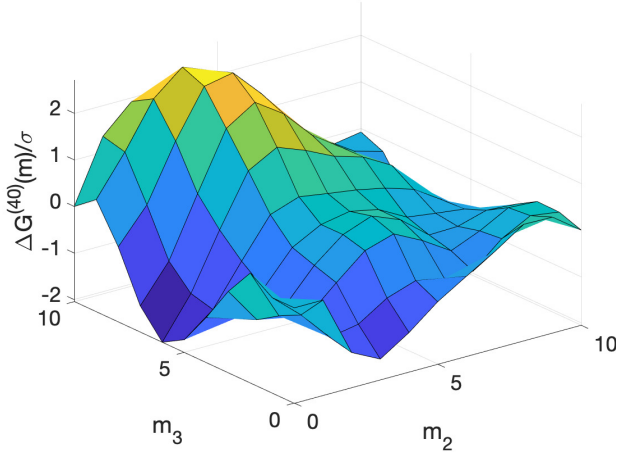


Figure 5. Normalized difference of simulation versus test distribution, for a four-fold partition and a thermal input. Results are for $\Delta\mathcal{G}_{(10,10,10,10)}^{(40)}(\mathbf{m})/\sigma_m$ vs \mathbf{m} , with sample numbers of $S = 1.2 \times 10^6$. Data is given as a two-dimensional planar slice in (m_2, m_3) of a four-dimensional probability space, with $m_1 = 6$ and $m_4 = 5$. No cut off was required here.

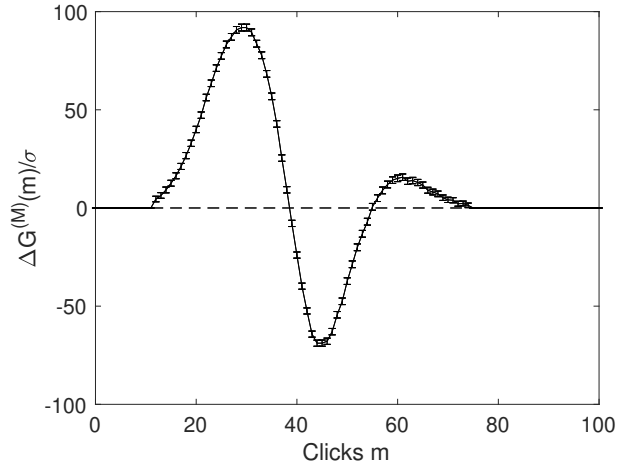


Figure 6. Normalized difference of simulation versus experimental count distribution, *excluding* decoherence. Results are for $\Delta\mathcal{G}_M^{(M)}(m)/\sigma_m$ vs m , with sample numbers of $S = 1.2 \times 10^6$. The error bars indicate errors due to finite experimental counts plus theoretical sampling errors. The results are cut off for all counts less than 10.

EXAMPLE: GROUPED TOTAL COUNTS IN GBS

normalized and thermal inputs. Both unitary and lossy transmission matrices were used, and homogeneous or inhomogeneous squeezed inputs. For 40×40 and 100×100 matrices, 9 different types of moment were tested with up to four-dimensional binning.

A typical example output is plotted in Fig (5), which shows a test for a thermalized input with $r = \epsilon = 1$ and $N = M = 40$, using a random unitary transmission matrix. The output is the probability for a $40 - th$ order correlation, binned four ways, to give $11^4 = 14641$ click patterns. The graph of the normalized error is a two-dimensional slice in the $m_2 - m_3$ plane, with $m_1 = 6$ and $m_4 = 5$.

Plotted data was all within $\pm 2\sigma$ of exact values. The χ^2 test gave $\chi_s^2/k = 0.99$ in 9935 significant data points restricted to $\mathcal{G} > 10^{-7}$, out of 14641 possible click patterns. These results show complete agreement with the analytic probability model.

For each matrix size, 68 distinct tests with up to 10^4 significant points were carried out, using P, Q or Wigner phase-space methods. Probability cutoffs were used of $\mathcal{G} > 10^{-7}$, with 1.2×10^6 total samples, since small probabilities were non-Gaussian. This effect is reduced by increasing the ensemble size. The overall result for 100×100 matrices was $\chi_s^2/k = 1.2 \pm 0.2$. This agrees with analytic tests, with evidence for nearly Gaussian sampling errors.

As a relevant example, treated in the main text, we consider the case of grouped 100-th order correlations in a GBS experiment, as compared to a phase-space simulation. We wish to compare two hypotheses. The first, \mathcal{H}_0 , is that the correlations are given by the experimental squeezing and transmission matrices. The second, \mathcal{H}_1 , is that there is additional decoherence, modeled by an thermal fraction ϵ , with an unchanged photon number.

In both cases, the experimental counts are the same. However, graphing the raw experimental and theoretical count probabilities is not useful for comparative purposes. Due to the high accuracy of the data, with over 10^7 total counts, it is much more useful to graph the normalized differences between theory and experiment:

$$z_m = \frac{\Delta\mathcal{G}_M^{(M)}(m)}{\sigma_m} = \frac{\mathcal{G}_m - \mathcal{G}_m^e}{\sigma_m}$$

Figure (6), shows the normalized discrepancy between theory and experiment in $\mathcal{G}_m = \mathcal{G}_M^{(M)}(m)$, with a simulation having no decoherence. An inspection of the graph shows very significant differences between the theoretical and experimental count probabilities, with $|z| \gg 1$. For the null hypothesis \mathcal{H}_0 , one finds an extremely large χ^2 value of 1.34×10^5 , out of 63 valid data points having more than 10 counts. The total ratio of $\chi_c^2/k = 2.1 \times 10^3 \gg 1$.

In summary, without any decoherence, the experiments strongly disagree with a simple, coherent GBS model. The hypothesis of no decoherence, apart from losses, has a vanishingly small probability. The hypothesis of a fully thermal model is far less likely still. With this model, the

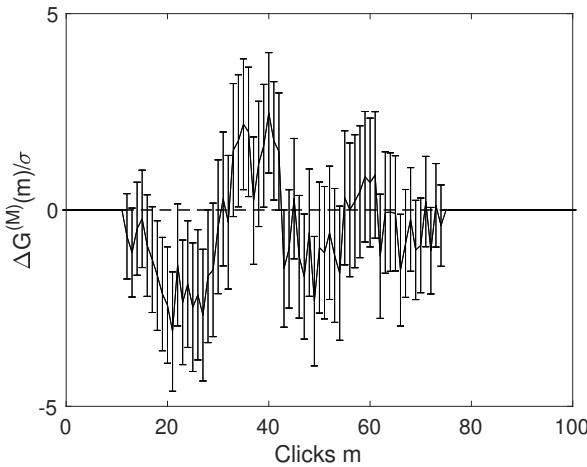


Figure 7. Normalized difference of simulation versus experimental count distribution, *including* decoherence. Results are for $\Delta G_M^{(M)}(m) / \sigma_m$ vs m , with sample numbers of $S = 1.2 \times 10^6$. The error bars indicate RMS errors due to finite experimental counts, plus theoretical sampling errors (which are 50% smaller). The results are cut off for counts less than 10, where the experimental data is less reliable. The maximum error is reduced by about two orders of magnitude compared to the coherent model.

total ratio of $\chi_{th}^2/k = 3.62 \times 10^4 \gg 1$. Hence, the output is easily distinguishable from a thermal one [64].

Figure (7), shows the differences in $\mathcal{G}_m = \mathcal{G}_M^{(M)}(m)$, between experiment and a simulation with a relatively small decoherence of $\epsilon = 0.138$, as described in the main text. The experimental transmission amplitude was increased by 0.61% (reduced absorption) to improve the fit. This is an even smaller correction. The new graph shows only minor statistical differences between the theoretical and experimental count probabilities, with $|z| \sim O(1)$, as expected.

For the hypothesis \mathcal{H}_1 , of additional decoherence, one finds a small χ^2 value of 77 ± 20 . The total ratio is $\chi^2/\epsilon = 1.27 = O(1)$, about 2000 times lower than before. This indicates that the hypothesis of additional decoherence is compatible with experimental measurements. *These results show excellent agreement with a model of GBS including a small thermal decoherence.*

The phase-space errors here were 50% less than the experimental errors, and could be easily reduced further. There were 40 times more experimental than theoretical samples. This is therefore at least as efficient as experiment. The error ratio depends on the relative sample numbers and the observations. The simulations presented typically took 60s with a 14 core desktop computer.

The same technique is applicable to *any* measurable distribution, including lower order correlations and multiple partitions. We plot an example of a doubly parti-

tioned probability distribution in the main text. This has similar properties, with a distribution very close to the experimental one. Due to the unprecedented accuracy of these tests, further adjustment in the measured transmission or squeezing is typically required for an optimal fit.

In general it is possible to check the GBS hypothesis for any set of parameters and observational moments. As we show here, the grouped measurable probability distributions of GBS experimental data can be simulated to extremely high accuracy. We have simulated correlation orders from first up to 16,000th order. The computational time depends on the complexity of extraction of the binned correlations, and on the error requirements.

There are an exponentially large number of correlation tests possible, as there are with any RNG. Thus, to disprove a classical mock-up, one can simply use a large, randomly chosen subset of tests of all orders. Just as with other RNG tests, it is increasingly unlikely that a range of statistical tests like this could be faked.

N-PARTITE ENTANGLEMENT

We will next consider simulating the M -partite entangled state that is created by first generating a two-mode Einstein-Podolsky-Rosen (EPR) correlated state, using one or two squeezed inputs on a beam splitter [65], described in the main text. Once the EPR state has been created, the system is passed through a further $M - 2$ beam splitters to create a state with genuine M -partite entanglement [41, 43].

We consider M modes labelled by $j = 1, \dots, M$, with associated boson destruction operators \hat{a}_j . We define the quadrature phase amplitudes of each mode as $\hat{x}_i = \hat{a}_i + \hat{a}_i^\dagger$ and $\hat{p}_i = \frac{1}{i}(\hat{a}_i - \hat{a}_i^\dagger)$, in an appropriate rotating frame. The set-up is M inputs \hat{a}_j^{in} , with the first two inputs being orthogonally squeezed vacuum states. In particular, \hat{a}_2^{in} is a squeezed vacuum input with $\Delta^2 \hat{x}_2^{in} = e^{-2r}$, and \hat{a}_1^{in} is squeezed vacuum input with $\Delta^2 \hat{p}_1^{in} = e^{-2r}$. Here $r > 0$ is the squeezing parameter. All other inputs are vacuum states, implying $\Delta^2 \hat{x}_j^{in} = \Delta^2 \hat{p}_j^{in}$. The inputs are combined across a total of $M - 1$ beam splitters. Here, we have used the notation $\Delta^2 \hat{x}$ to mean the variance of \hat{x} , i.e. $\Delta^2 \hat{x} = (\Delta \hat{x})^2 = \langle \hat{x}^2 \rangle - \langle \hat{x} \rangle^2$.

First, to create two-mode EPR entanglement, the inputs 1 and 2 are combined across a beam splitter $BS1$ as below, with reflectivity R_1^2 and $T_1^2 = 1 - R_1^2$, according to

$$\begin{aligned} \hat{a}_1^{(1)} &= R_1 \hat{a}_1^{in} + T_1 \hat{a}_2^{in} \\ \hat{a}_2^{(1)} &= T_1 \hat{a}_1^{in} - R_1 \hat{a}_2^{in}. \end{aligned} \quad (18)$$

The output of \hat{a}_1 is $\hat{a}_1^{(1)}$. It is straightforward to show

that the two output fields are EPR correlated i.e.

$$\begin{aligned}\Delta^2(\hat{x}_1 - \hat{x}_2^{(1)}) &= 2e^{-2r} \\ \Delta^2(\hat{p}_1 + \hat{p}_2^{(1)}) &= 2e^{-2r}.\end{aligned}\quad (19)$$

For large r , both variances become zero. EPR entanglement can also be created from one squeezed input to give [65]

$$\begin{aligned}\Delta^2(\hat{x}_1 - \hat{x}_2^{(1)}) &= 2e^{-r} \\ \Delta^2(\hat{p}_1 + \hat{p}_2^{(1)}) &= 2e^{-r}.\end{aligned}\quad (20)$$

To generate multipartite entanglement, the field $\hat{a}_2^{(1)}$ is combined across with a second *BS2* with reflectivity R_2^2 and $T_2^2 = 1 - R_2^2$, according to [41, 43]

$$\begin{aligned}\hat{a}_2^{(2)} &= R_2 \hat{a}_2^{(1)} + T_2 \hat{a}_3^{in} \\ \hat{a}_3^{(2)} &= T_2 \hat{a}_2^{(1)} - R_2 \hat{a}_3^{in}.\end{aligned}\quad (21)$$

The output of field \hat{a}_2 is $\hat{a}_2^{(2)}$. For $M = 3$, there are only two BS, and the output of \hat{a}_3 is $\hat{a}_3^{(2)}$. For $M = 4$, the process continues with another beam splitter

$$\begin{aligned}\hat{a}_3^{(3)} &= (R_3 \hat{a}_3^{(2)} + T_3 \hat{a}_4^{in}) \\ \hat{a}_4^{(3)} &= (T_3 \hat{a}_3^{(2)} - R_3 \hat{a}_4^{in}).\end{aligned}\quad (22)$$

The output of mode \hat{a}_3 is $\hat{a}_3^{(3)}$ and the output of mode \hat{a}_4 is $\hat{a}_4^{(3)}$.

Continuing, it is possible to select the reflectivities of the string of beam splitters so that we obtain

$$\begin{aligned}\Delta^2(x_1 - \frac{1}{\sqrt{M-1}}(x_2 + x_3 + \dots x_M)) &= 2e^{-2r} \\ \Delta^2(\hat{p}_1 + \frac{1}{\sqrt{M-1}}(\hat{p}_2 + \hat{p}_3 + \dots \hat{p}_M)) &= 2e^{-2r},\end{aligned}\quad (23)$$

which gives genuine M -partite entanglement. This is done selecting for the beam splitters, $R_{M-1}^2 = 1/2$, $R_{M-2}^2 = \frac{1}{3}$, $R_{M-j}^2 = \frac{1}{j+1}$ for $j < M - 1$, a [41, 43], with $R_1^2 = 1/2$.

Unitary matrix

The corresponding unitary matrix is obtained by first introducing a vector of reflection amplitudes, defined by

$$\begin{aligned}R_j &= \sqrt{\frac{1}{M-j+1}}, \quad 1 < j \leq M \\ R_1 &= \sqrt{\frac{1}{2}} \\ T_j &= \sqrt{1 - R_j^2}.\end{aligned}\quad (24)$$

We may express the transformation of the M input modes into M genuinely entangled output modes as a unitary matrix U . Thus the output modes are

$$\begin{pmatrix} \hat{a}_1^{out} \\ \hat{a}_k^{out} \\ \dots \\ \hat{a}_M^{out} \end{pmatrix} = U \begin{pmatrix} \hat{a}_1^{in} \\ \hat{a}_k^{in} \\ \dots \\ \hat{a}_M^{in} \end{pmatrix}.\quad (25)$$

Defining $R_0 = -1$ and $R_M = 1$, the elements U_{kj} of the $M \times M$ unitary U matrix for $j, k = 1, \dots, M$ are given by:

$$\begin{cases} U_{kj} = 0 & j > k + 1 \\ U_{kj} = R_1 & j = k = 1 \\ U_{kk} = -R_k R_{k-1} & \\ U_{k(k+1)} = T_k & k < M \\ U_{kj} = -R_k T_{k-1} \dots T_j R_{j-1} & 1 \leq j < k + 1 \end{cases}.\quad (26)$$

SIMULATING N-PARTITE ENTANGLEMENT

This type of experiment is also readily simulated using phase-space methods. The details are different to the saturating photo-detector scenario explained in the second section, above. This case demonstrates the high efficiency of Wigner phase-space methods for simulating quadrature measurements. This, of course, is a completely different type of measurement to the click detection often used in GBS.

Let $\hat{u} = \hat{x}_1 - \frac{1}{\sqrt{M-1}}(\hat{x}_2 + \hat{x}_3 + \dots + \hat{x}_M)$ and $\hat{v} = \hat{p}_1 + \frac{1}{\sqrt{M-1}}(\hat{p}_2 + \hat{p}_3 + \dots + \hat{p}_M)$, then the observation of

$$(\Delta \hat{u})^2 (\Delta \hat{v})^2 < \frac{4}{(M-1)^2} \quad (27)$$

confirms M -partite entanglement for all M . The observation of

$$(\Delta \hat{u})^2 + (\Delta \hat{v})^2 < \frac{4}{M-1} \quad (28)$$

also confirms M -partite entanglement for all M . Here, we use notation $\Delta \hat{x} = \sqrt{\text{Var}(\hat{x})} = \sqrt{\langle \hat{x}^2 \rangle - \langle \hat{x} \rangle^2}$. A detailed proof of these threshold points will be given elsewhere.

Figure (8), shows the result of a Wigner simulation of multipartite entanglement, plotted against the number of input modes, for $r = 3$ and $S = 1.2 \times 10^6$ samples. The total ratio of $\chi^2/k = 0.965 < 1$, for 99 data points, showing that the simulation is consistent with the analytic result. The simulation error bars are $O(10^{-5})$.

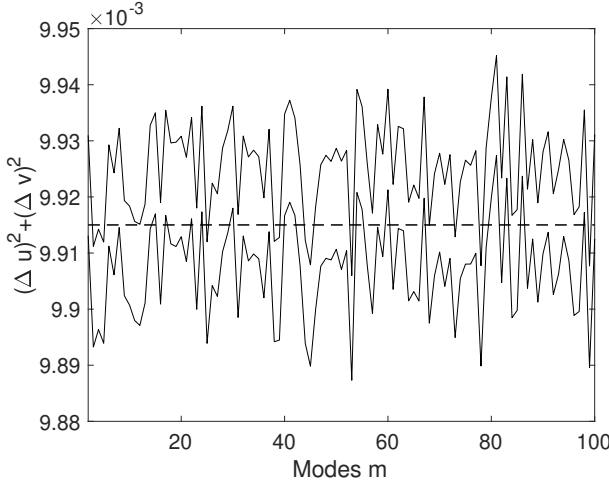


Figure 8. Graph of simulated multipartite entanglement product against number of entangled modes, using the Wigner representation. Sample numbers were $S = 1.2 \times 10^6$ with an input squeezing of $r = 3$, using a unitary matrix and pure state inputs. The upper and lower solid lines are sampling errors, the dashed line the exact result. Sampling errors here are about $\pm 1.0 \times 10^{-5}$.

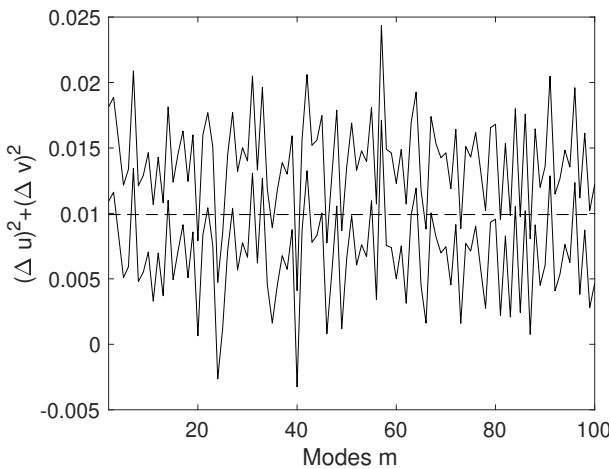


Figure 9. Graph of simulated multipartite entanglement product in the $+P$ representation, with sample numbers of $S = 1.2 \times 10^6$ and squeezing of $r = 3$, using a unitary matrix and pure state inputs. The upper and lower solid lines are sampling errors, the dashed line the exact result. Sampling errors here are much larger: about $\pm 2.0 \times 10^{-3}$.

The threshold for the signature in this case is 0.0404 at $M = 100$, so the criterion is satisfied.

This level of precision are not obtained for all phase-space methods. Figure (8), shows the result of a positive- P simulation of multipartite entanglement, otherwise identical to figure (8). Here the total chi-squared ratio of $\chi^2/k = 0.98 < 1$, for 99 independent points, indicating agreement with the analytic result. The error bars are now $\pm 2 \times 10^{-3}$, which is 200 times larger.

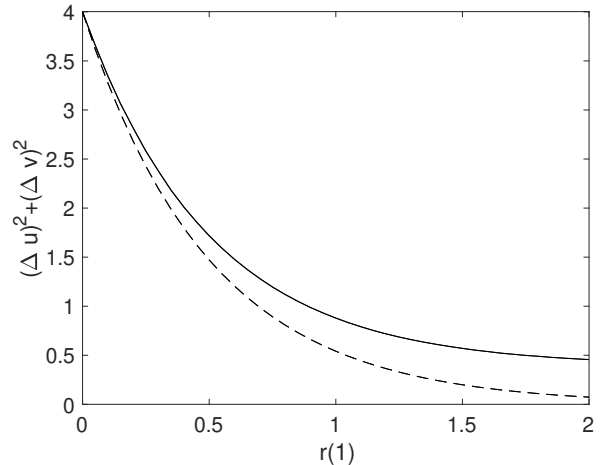


Figure 10. Graph of simulated multipartite entanglement product in the Wigner representation, versus squeezing r , with an input amplitude transmission of $t = 0.95$ and $M = 40$ modes. The required threshold of 0.44 is not reached even with a large squeezing of $r = 2$. Other parameters as in Fig (8). Sampling errors are negligible: $\pm 10^{-6}$. This shows that input coupling losses can destroy the multi-partite entanglement signature.

Similar large error bars are found for the Q -function representation. In both cases, one must add or subtract corrections to transform the variance to the required symmetric ordering. This leads to larger sampling errors.

While this result is obtainable analytically, simulations can include effects like losses, decoherence and inhomogeneity. These all impact the amount of input squeezing required in realistic experiments. A simple example is shown in Fig (10) which simulates an input coupling amplitude transmission of 0.95. This is sufficient to prevent the multipartite signature from being achieved for an $M = 40$ network, with $r = 2$.

- [1] S. Scheel, in *Quantum Information Processing*, edited by T. Beth and G. Leuchs (Wiley-VCH, Weinheim, 2005) Chap. 28, pp. 382–392.
- [2] S. Aaronson, Proceedings of the Royal Society of London A: Mathematical, Physical and Engineering Sciences **467**, 3393 (2011).
- [3] M. A. Broome, A. Fedrizzi, S. Rahimi-Keshari, J. Dove, S. Aaronson, T. C. Ralph, and A. G. White, *Science* **339**, 794 (2013).
- [4] A. Crespi, R. Osellame, R. Ramponi, D. J. Brod, E. F. Galvao, N. Spagnolo, C. Vitelli, E. Maiorino, P. Mataloni, and F. Sciarrino, *Nature photonics* **7**, 545 (2013).
- [5] M. Tillmann, B. Dakic, R. Heilmann, S. Nolte, A. Szameit, and P. Walther, *Nature photonics* **7**, 540 (2013).
- [6] J. B. Spring, B. J. Metcalf, P. C. Humphreys, W. S. Kolthammer, X.-M. Jin, M. Barbieri, A. Datta, N. Thomas-Peter, N. K. Langford, D. Kundys, *et al.*,

Science **339**, 798 (2013).

[7] N. Spagnolo, C. Vitelli, M. Bentivegna, D. J. Brod, A. Crespi, F. Flamini, S. Giacomini, G. Milani, R. Ramponi, P. Mataloni, *et al.*, Nature Photonics **8**, 615 (2014).

[8] A. Crespi *et al.*, Nat. Commun. **7**, 10469 (2016).

[9] A. P. Lund, A. Laing, S. Rahimi-Keshari, T. Rudolph, J. L. O'Brien, and T. C. Ralph, Phys. Rev. Lett. **113**, 100502 (2014).

[10] C. S. Hamilton, R. Kruse, L. Sansoni, S. Barkhofen, C. Silberhorn, and I. Jex, Phys. Rev. Lett. **119**, 170501 (2017).

[11] N. Quesada, J. M. Arrazola, and N. Killoran, Physical Review A **98**, 062322 (2018).

[12] R. Kruse, C. S. Hamilton, L. Sansoni, S. Barkhofen, C. Silberhorn, and I. Jex, Physical Review A **100**, 032326 (2019).

[13] C. M. Caves, Physical Review D **23**, 1693 (1981).

[14] L. McCuller, C. Whittle, D. Ganapathy, K. Komori, M. Tse, A. Fernandez-Galiana, L. Barsotti, P. Fritschel, M. MacInnis, F. Matichard, K. Mason, N. Mavalvala, R. Mittleman, H. Yu, M. E. Zucker, and M. Evans, Physical Review Letters **124**, 171102 (2020).

[15] K. R. Motes, J. P. Olson, E. J. Rabeaux, J. P. Dowling, S. J. Olson, and P. P. Rohde, Phys. Rev. Lett. **114**, 170802 (2015).

[16] Z.-E. Su, Y. Li, P. P. Rohde, H.-L. Huang, X.-L. Wang, L. Li, N.-L. Liu, J. P. Dowling, C.-Y. Lu, and J.-W. Pan, Phys. Rev. Lett. **119**, 080502 (2017).

[17] M. Chen, N. C. Menicucci, and O. Pfister, Phys. Rev. Lett. **112**, 120505 (2014).

[18] J. Roslund, R. M. De Araujo, S. Jiang, C. Fabre, and N. Treps, Nature Photonics **8**, 109 (2014).

[19] J.-i. Yoshikawa, S. Yokoyama, T. Kaji, C. Sornphiphatphong, Y. Shiozawa, K. Makino, and A. Furusawa, APL Photonics **1**, 060801 (2016).

[20] A. Marandi, Z. Wang, K. Takata, R. L. Byer, and Y. Yamamoto, Nature Photonics **8**, 937 (2014).

[21] T. Inagaki, Y. Haribara, K. Igarashi, T. Sonobe, S. Tamate, T. Honjo, A. Marandi, P. L. McMahon, T. Umeki, K. Enbutsu, *et al.*, Science **354**, 603 (2016).

[22] Y. Yamamoto, K. Aihara, T. Leleu, K.-i. Kawarabayashi, S. Kako, M. Fejer, K. Inoue, and H. Takesue, npj Quantum Information **3**, 1 (2017).

[23] H.-S. Zhong, H. Wang, Y.-H. Deng, M.-C. Chen, L.-C. Peng, Y.-H. Luo, J. Qin, D. Wu, X. Ding, Y. Hu, *et al.*, Science **370**, 1460 (2020).

[24] M. J. Bremner, A. Montanaro, and D. J. Shepherd, Phys. Rev. Lett. **117**, 080501 (2016).

[25] S. Boixo, S. V. Isakov, V. N. Smelyanskiy, R. Babbush, N. Ding, Z. Jiang, M. J. Bremner, J. M. Martinis, and H. Neven, Nature Physics **14**, 595 (2018).

[26] F. Arute, K. Arya, R. Babbush, D. Bacon, J. C. Bardin, R. Barends, R. Biswas, S. Boixo, F. G. Brandao, D. A. Buell, *et al.*, Nature **574**, 505 (2019).

[27] D. Shepherd and M. J. Bremner, Proceedings of The Royal Society A: Mathematical, Physical and Engineering Sciences **465**, 1413 (2009).

[28] D. Hangleiter, M. Kliesch, J. Eisert, and C. Gogolin, Phys. Rev. Lett. **122**, 210502 (2019).

[29] D. Phillips, M. Walschaers, J. Renema, I. Walmsley, N. Treps, and J. Sperling, Physical Review A **99**, 023836 (2019).

[30] N. Quesada and J. M. Arrazola, Physical Review Research **2**, 023005 (2020).

[31] Y. Li, M. Chen, Y. Chen, H. Lu, L. Gan, C. Lu, J. Pan, H. Fu, and G. Yang, arXiv preprint arXiv:2009.01177 (2020).

[32] D. J. Brod, E. F. Galvão, A. Crespi, R. Osellame, N. Spagnolo, and F. Sciarrino, Advanced Photonics **1**, 034001 (2019).

[33] B. Opanchuk, L. Rosales-Zárate, M. D. Reid, and P. D. Drummond, Physical Review A **97**, 042304 (2018).

[34] H. Qi, D. J. Brod, N. Quesada, and R. García-Patrón, Physical review letters **124**, 100502 (2020).

[35] K. Pearson, Biometrika **8**, 250 (1911).

[36] D. E. Knuth, *Art of computer programming, volume 2: Seminumerical algorithms* (Addison-Wesley Professional, 2014).

[37] W. Diffie and M. Hellman, IEEE transactions on Information Theory **22**, 644 (1976).

[38] P. D. Drummond and C. W. Gardiner, J. Phys. A **13**, 2353 (1980).

[39] E. Wigner, Physical Review **40**, 749 (1932).

[40] B. Opanchuk, L. Rosales-Zárate, M. D. Reid, and P. D. Drummond, Optics Letters **44**, 343 (2019).

[41] P. van Loock and A. Furusawa, Physical Review A **67**, 052315 (2003).

[42] J. Sperling and W. Vogel, Physical review letters **111**, 110503 (2013).

[43] R. Y. Teh and M. D. Reid, Physical Review A **90**, 062337 (2014).

[44] A. Coelho, F. Barbosa, K. Cassemiro, A. Villar, M. Martinelli, and P. Nussenzveig, Science **326**, 823 (2009).

[45] S. Armstrong, M. Wang, R. Y. Teh, Q. Gong, Q. He, J. Janousek, H.-A. Bachor, M. D. Reid, and P. K. Lam, Nature Physics **11**, 167 (2015).

[46] H. P. Yuen, Physical Review A **13**, 2226 (1976).

[47] H. Vahlbruch, M. Mehmet, K. Danzmann, and R. Schnabel, Physical Review Letters **117**, 110801 (2016).

[48] M. Hillery, R. O'Connell, M. Scully, and E. Wigner, Physics Reports **106**, 121 (1984).

[49] P. D. Drummond, C. W. Gardiner, and D. F. Walls, Phys. Rev. A **24**, 914 (1981).

[50] P. D. Drummond and S. Chaturvedi, Physica Scripta **91**, 073007 (2016).

[51] R. J. Glauber, Phys. Rev. **130**, 2529 (1963).

[52] J. Janszky and A. V. Vinogradov, Physical review letters **64**, 2771 (1990).

[53] P. D. Drummond and B. Opanchuk, Physical Review Research **2**, 033304 (2020).

[54] M. G. Raymer, P. D. Drummond, and S. J. Carter, Optics letters **16**, 1189 (1991).

[55] H. Fearn and M. Collett, Journal of Modern Optics **35**, 553 (1988).

[56] K. E. Cahill and R. J. Glauber, Physical Review **177**, 1882 (1969).

[57] E. Wigner, Phys. Rev. **40**, 749 (1932).

[58] K. Husimi, Proc. Phys. Math. Soc. Jpn. **22**, 264 (1940).

[59] M. Olsen and A. Bradley, Optics Communications **282**, 3924 (2009).

[60] C. Gardiner, *Handbook of Stochastic Methods for Physics, Chemistry, and the Natural Sciences*, Springer complexity (Springer, 2004).

[61] P. D. Drummond, B. Opanchuk, L. Rosales-Zárate, M. D. Reid, and P. J. Forrester, Physical Review A **94**, 042339 (2016).

[62] K. Pearson, The London, Edinburgh, and Dublin Philosophical Magazine and Journal of Science **50**, 157 (1900).

- [63] A. L. Rukhin, J. Soto, J. R. Nechvatal, M. E. Smid, E. B. Barker, S. D. Leigh, M. Levenson, M. Vangel, D. L. Banks, *et al.*, A statistical test suite for random and pseudorandom number generators for cryptographic applications (2010).
- [64] S. Aaronson and A. Arkhipov, *Quantum Info. Comput.* **14**, 1383 (2014).
- [65] M. D. Reid, *Phys. Rev. A* **40**, 913 (1989).
- [66] P. A. M. Dirac, *Rev. Mod. Phys.* **17**, 195 (1945).
- [67] J. T. Roscoe and J. A. Byars, *Journal of the American Statistical Association* **66**, 755 (1971).
- [68] K. Pearson, *Biometrika* , 457 (1932).
- [69] B. Gupt, J. M. Arrazola, N. Quesada, and T. R. Bromley, *Quantum Information Processing* **19**, 1 (2020).